Fluoroalcohol-Induced Modulation of the Pathway of Amyloid Protofibril Formation by Barstar[†]

Amrita Sekhar and Jayant B. Udgaonkar*

National Centre for Biological Sciences, Tata Institute of Fundamental Research, Bangalore 560065, India

ABSTRACT: To understand how the conformational heterogeneity of protofibrils formed by any protein, as well as the mechanisms of their formation, are modulated by a change in aggregation conditions, we studied the formation of amyloid protofibrils by barstar at low pH by multiple structural probes in the presence of hexafluoroisopropanol (HFIP). In the presence of 10% HFIP, aggregation proceeds with the transient formation of spherical oligomers and leads to the formation of both protofibrils and fibrils. Curly short protofibrils and fibrils are seen to form early during the aggregation reaction, and both are seen to grow gradually in length during the course of the reaction. Atomic force microscopy images reveal that the HFIP-induced protofibrils are long ($\sim$300 nm in length), curly, and beaded and appear to be composed primarily of β-sheet bilayers, with heights of $\sim$2.4 nm. The protofibrils formed in the presence of HFIP differ in both their structures and their stabilities from the protofibrils formed either in the absence of alcohol or in the presence of a related alcohol, trifluoroethanol (TFE). Aggregation appears to proceed via an isodesmic polymerization mechanism. Internal structure in the growing aggregates changes in two stages during protofibril formation. In the first stage, an α-helix-rich oligomeric intermediate is formed. In the second stage, the level of β-sheet structure increases at the expense of some α-helical structure. The second stage itself appears to occur in two distinct steps. The creation of thioflavin T binding sites occurs concomitantly with aggregate elongation and is seen to precede the change in secondary structure. The long straight fibrils with characteristic heights of 8–10 nm, which form in the course of the HFIP-induced aggregation reaction, have not been observed to form either in the absence of alcohol or in the presence of TFE.

Protein aggregation is a commonly observed cellular phenomenon (*1−9*). Aggregates can vary in their morphologies and shapes, as well as in the details of their structures (*10−15*). A well-studied class of protein aggregates is the class of amyloid fibrils. Amyloid fibrils are highly organized fibrillar states with well-defined internal structures (*16, 17*). Many proteins have been shown to form amyloid fibrils under various conditions. While some fibrils such as those formed by the *Escherichia coli* protein curlin (*18*), those present in spider silk (*19*), and those formed by the mammalian protein Pmel17 (*20*) are beneficial to the host, there are many instances in which amyloid fibril formation is associated with disease (*21*). The best-studied examples include the group of diseases called prion diseases caused by the aggregation of the prion protein (*22−24*) and Alzheimer's disease caused by the aggregation of the Aβ peptide (*25, 26*).

Amyloid fibril formation has been studied in considerable detail using both in vitro and in vivo approaches. The structures of amyloid fibrils formed by different proteins have been studied using many techniques, including atomic force microscopy (AFM),[1] X-ray diffraction, and solid state nuclear magnetic resonance (NMR) spectroscopy (*27, 28*). Typically, fibrils are $\sim$10−12 nm wide and are composed of a variable number of protofilaments that either twist around each other or associate laterally to give rise to fibrils (*29*). The fibrils are characterized by the presence of a cross β-motif in which the β-sheets lie parallel and the β-strands composing the sheets run perpendicular to the fibril axis (*15, 17, 30−32*).

The mechanism of amyloid formation has been investigated for many proteins (*33−37*). For a large number of proteins, a large number of intermediate aggregates with different morphologies have been observed to form transiently. These include spherical oligomers, protofibrils (both curly and rodlike), and annular protofibrils (*10, 14*). A number of studies have implicated the intermediates formed on the aggregation pathway as the toxic species (*7, 38*). Hence, an investigation of the mechanisms governing protofibril formation and their structural features is important.

Amyloid fibrils are also found to possess a great deal of structural heterogeneity (*39, 40*). Fibrils formed by the same protein under different conditions can have very different morphologies. In the case of fibrils formed by Aβ, AFM and solid state NMR studies have shown the existence of fibrils with different morphologies that result from a difference in their internal structures. The different fibril morphologies also show different toxicities (*41*). In another study of α-synuclein aggregation,

*To whom correspondence should be addressed. Telephone: 91-80-23666150. Fax: 91-80-23636462. E-mail: jayant@ncbs.res.in.

[1]Abbreviations: HFIP, hexafluoroisopropanol; TFE, trifluoroethanol; AFM, atomic force microscopy; TEM, transmission electron microscopy; ATR-FTIR, attenuated total reflectance Fourier transform infrared; CD, circular dichroism; ThT, thioflavin T; θ_{216}, ellipticity at 216 nm; R_H, hydrodynamic radius; SI, scattering intensity; DLS, dynamic light scattering; NMR, nuclear magnetic resonance; CMC, critical micelle concentration; NDP, nucleation-dependent polymerization.

distinct fibril morphologies were found under the same experimental conditions, which differed in their internal structures as determined by solid state NMR (*27*). Conformational heterogeneity has also been shown for the same sequence of the prion protein, thereby emphasizing the point that the ability to form different fibrillar structures is an intrinsic property of protein aggregation reactions (*42*). Nevertheless, the origin of conformational polymorphism in fibrils remains poorly understood.

In this report, the heterogeneity in protofibril structures formed by the model protein barstar, from the bacterium *Bacillus amyloliquefaciens*, has been studied. It is known that proteins differing widely in their native structures form protofibrils that share common structural features (*43*), and the study of amyloid protofibril and fibril formation by a model protein such as barstar is important because the extensive knowledge already obtained on its unfolding pathway (*44–48*) can reveal insights into how such aggregation begins. When barstar is partially unfolded at pH 2.7, it oligomerizes to form a 16-mer called the A form (*44*), which has been characterized by multidimensional NMR spectroscopy (*49*). Protofibril formation at low pH has been well-studied (*35, 50–53*) and has been shown to proceed from the A form (*44*). This process is extremely slow at room temperature, but its rate is greatly enhanced at higher temperatures (*35, 50*). Protofibrils appear to form directly from the A form and appear to be composed of a β-sheet bilayer. They have been characterized extensively by the use of time-resolved fluorescence methods, which have delineated the structured cores of the protofibrils as well as of the A form (*53, 54*). The final structure formed at the end of the aggregation reaction has been to shown to depend on the aggregation condition (*52*). The observation that the mechanism of aggregation of barstar (*35, 50*) is similar in many respects to that of amyloid-β (*55, 56*), the mouse prion protein (*36, 57*), and other proteins (*37*) underlines the utility of using barstar as a model protein for investigating the mechanistic origin of the conformational heterogeneity seen in protofibrils and fibrils.

Alcohols have been used extensively in aggregation studies as they are able to perturb the native state by weakening hydrophobic interactions (*58*). Water/alcohol mixtures have reduced polarity, and the effectiveness of an alcohol in its ability to perturb protein structure and stability is consequently related to its dielectric constant (*59, 60*). Fluoroalcohols are more effective than ordinary alcohols in disrupting tertiary interactions in folded proteins as they lower solvent polarity by a more drastic extent and they favor the formation of α-helical structures by promoting intramolecular hydrogen bonding. It has been suggested that hexafluoroisopropanol (HFIP) is more effective than trifluoroethanol (TFE) in mediating these effects because of the presence of three additional fluorine atoms, which makes it ∼34-fold more acidic than TFE (*61*).

HFIP is known to favor the formation of aggregates in a concentration-dependent manner. At optimal concentrations, it is very effective in promoting protein aggregation by maintaining a critical balance between hydrophobic and polar interactions (hydrogen bonding), both of which are essential for fibril formation to occur (*62*). Many studies suggest that HFIP preferentially interacts with the polypeptide backbone (*62, 63*), and it has also been suggested (*60*) that, unlike TFE, HFIP can preferentially bind to the polypeptide chain via hydrophobic interactions. It should be noted that at very high concentrations, HFIP destabilizes aggregates by weakening the hydrophobic interactions that are needed for intermolecular association, and

consequently, solutions containing high concentrations of HFIP are frequently used to dissolve protein aggregates (*64*). Both HFIP and TFE are used to mimic the effect of membranes on proteins.

In this study, it is found that the A form of barstar aggregates in the presence of 10% HFIP. Higher-order spherical oligomeric intermediates are first formed, and then wormlike protofibrils. These protofibrils appear to be composed of a β-sheet bilayer, as seen from their heights on AFM mica. The protofibrils are ∼300 nm in length and are much longer than those formed in the absence of HFIP. Once formed, they are very stable and resistant to disaggregation. Formation of protofibrils from the A form proceeds via an intermediate oligomeric form rich in α-helical content, and the subsequent kinetics of protofibril formation is sigmoidal, with a very weak lag phase. Interestingly, the protofibrils formed in the presence of HFIP differ from those formed in its absence, or in the presence of TFE, in their final structure as seen by their lengths determined by AFM, in their DLS size distributions, and in their far-UV CD spectra. They also show very different stabilities under disaggregating conditions. Furthermore, typical long straight fibrils with heights of 8–10 nm are also seen to form in the presence of HFIP. Such fibrils have not been observed to form in the absence of HFIP or in the presence of TFE.

EXPERIMENTAL PROCEDURES

Protein Purification and Expression. The protein was expressed and purified as described previously (*44*). The sequence of the expressed protein is MKKAVINGEQIRSISDLHQTLK-KELALPEYYGENLDALWDCLTGWVEYPLVLEWRQFE-QSKQLTENGAESVLQVFREAKAEGCDITIILS. The purity of the protein was confirmed by SDS–PAGE and by mass spectrometry using a Micromass Q-TOF Ultima mass spectrometer. The mass of the protein was found to be as expected (10342 Da).

Buffer Solutions and Experimental Conditions. All the chemicals used in this study were of the highest quality grade available from Sigma. The buffers for all the experiments contained a 10-fold excess of dithiothreitol (DTT), over the protein concentration, to prevent any non-native disulfide bond formation by the two cysteine residues present in the protein (*65*). The absorbance at 280 nm was used to ascertain the protein concentration using an ε_{280} of 23000 M^{-1} cm^{-1} (*44*). For all the experiments, the protein was first dissolved in 20 mM Tris-HCl buffer (pH 8.0) and then diluted 10-fold into 50 mM glycine buffer to a final pH of 2.7. The protein was first incubated for 2 h at room temperature (25 °C). Previous studies (*35, 50*) have shown that the protein remains in the A form during this time, that no larger aggregates form, and that the subsequent apparent rate of formation of the A form is not affected when this time of incubation is varied between 30 min and 2 h. The process of protofibril formation was then initiated via addition of HFIP to a final concentration of 10% (v/v). The solution was subsequently incubated in a thermal block maintained at 25 °C. Aliquots were withdrawn at various times during the reaction for the ThT fluorescence measurements. For dynamic light scattering and ellipticity measurements, the protein solution containing 10% HFIP was transferred into a cuvette maintained at 25 °C, and the reaction was monitored at various times. Sufficient care was taken to avoid any variation in temperature arising from the use of different temperature-controlling units. For protofibril formation induced by TFE, the same protocol was followed. For the study of formation of protofibrils induced by heat, the protein

after incubation at room temperature for 2 h was transferred to a heating block maintained at 60 °C.

AFM images, as well as FTIR and far-UV CD spectra, of HFIP-induced, TFE-induced, and heat-induced protofibrils formed by 25 μM protein were obtained after aggregation for 2.6 h, 50 min, and 3.9 h, respectively, when each process was complete as measured by all the probes used in this study. Disaggregation experiments were conducted with protofibrils formed by the aggregation of 20 μM protein.

Thioflavin T Assay. A calculated amount of protein was added to 50 mM Tris-HCl buffer (pH 8) containing the thioflavin T (ThT) dye such that the final ratio of dye to protein in the assay solution was maintained at 2:1. This ratio was standardized on the basis of experiments in which the HFIP concentration in the assay was fixed and the ratio of ThT to protein was varied. It was found that the fluorescence signal decreased if the ratio was varied above 2:1 (data not shown). Even though the fluorescence signal was lower at a higher ratio of ThT to protein (5:1), the apparent rate constant for elongation was found to be the same (data not shown). At present, it is not known why the magnitude of the fluorescence signal decreases at a ThT:protein ratio exceeding 2:1 in the presence of HFIP, but it was found that the signal was strongly dependent on the amount of HFIP present in the assay solution (data not shown). Thus, irrespective of the protein concentration at which the aggregation reaction was conducted, the final HFIP concentration in the assay solution was always maintained at 2%. It should be noted that in previous studies of aggregation in the absence of HFIP, a ThT:protein ratio of 2:1 was found to be sufficient to saturate all dye binding sites (*35*). The final pH of the assay solution was always 7.9 ± 0.1. For the analysis of the ThT fluorescence data, the first three points of the 20 s trace at every time point were averaged and taken as the signal at that time point. ThT fluorescence measurements were conducted on a Fluoromax-3 spectrofluorimeter (Jobin Yvon). For the kinetic experiments, the sample was excited at 440 nm and the emission was monitored at 482 nm. The excitation and emission bandwidths were set to 1 and 10 nm, respectively. For each kinetic point, the signal was acquired for a total of 20 s after a mixing dead time of 10 s, with a signal averaging time of 2 s.

Circular Dichroism. Far-UV CD measurements were taken on Jasco J-720 and J-815 spectropolarimeters. The parameters used for the measurements of far-UV CD spectra were as follows: step resolution, 1 nm; scan speed, 100 nm/min; bandwidth, 1 nm; and response time, 2 s. A total of 25 scans were averaged. For all kinetic measurements, the ellipticity at 216 nm (θ_{216}) or 222 nm (θ_{222}) was monitored. For the analysis of the CD spectra, DichroWeb, an online server for deconvolution of CD spectra, was used (*66*). CDSSTR was used, and spectral deconvolution was conducted using reference set SP175 optimized for 190−240 nm (*67*).

Dynamic Light Scattering (*DLS*). The dynamic light scattering experiments were conducted on a DynaPro-99 unit (Wyatt Technology Corp.) using the procedure described previously (*35*). Briefly all the buffers at pH 8 and 2.7 were filtered through 0.02 μm filters from Whatman. The scattering intensity at right angles and its autocorrelation were acquired simultaneously using a laser at 829.4 nm to illuminate the sample. For the kinetic experiments, 15 acquisitions were collected at each time point. The acquisition time was set at 5 s, the signal-to-noise (S:N) threshold at 2.5, and the sensitivity at 70%. Data with uneven autocorrelation functions were excluded. The data were then resolved into a Gaussian distribution using DynaLS (Protein

Solutions Ltd.). The DynaLS results were further verified using a regularization algorithm. For the accurate determination of the hydrodynamic radii, the viscosities of the solutions used in the experiment were determined accurately by determining their refractive indices. Cumulant analysis (Wyatt Technology Corp.) was used to obtain the total scattering intensity.

Atomic Force Microscopy (*AFM*). AFM images of protofibrils induced by HFIP, heat, or TFE were obtained at different time points of aggregation of 25 μM protein. At the desired time points, the protein was diluted to a concentration of 0.3−0.5 μM in the aggregation buffer and applied to a freshly cleaved mica surface. After incubation for 3 min, the mica surface was washed with 0.22 μM filtered water at pH 2.7. The mica was then dried under vacuum for 1 h and imaged in noncontact mode on a PicoPlus AFM instrument with a small scanner with a window size of 12 μm × 12 μm (Molecular Imaging Inc.). The diameters of the protofibrils were determined by measuring the *Z* heights of the structures in the AFM images. The determination of each height distribution involved measurements of 150−200 individual protofibrils in ∼20 image frames. The height of each protofibril in turn was determined as the mean of the heights determined along its entire length. The widths and lengths were determined using the profile option in WSXM (*68*).

Transmission Electron Microscopy (*TEM*). TEM images of the protofibrils of 25 μM barstar induced by HFIP or TFE were obtained at 2.6 h and 55 min, respectively. These times correspond to $3/k$, where k is the apparent rate constant of elongation as determined from measurement of the far-UV CD kinetics. The protein was diluted to a concentration of 7.5 μM in pH 2.7 water, and a 5 μL aliquot was applied to a 400 mesh carbon-coated grid (Ted Pella) and allowed to adsorb onto the surface of the grid for 3 min. The grid was then washed three times (30 s each time) with filtered water at pH 2.7 and then stained with 2% uranyl acetate for 2 min. After being dried in air, the grids were examined on a Tecnai G^2 12 BioTwin electron microscope (FEI Co.) operating at 100 kV and equipped with a Gatan side mount 4k camera. Images were analyzed using the Gatan Digital Image micrograph software (version 1.8) and ImageJ version 1.4 (National Institutes of Health).

Fourier Transform Infrared Spectroscopy (*FTIR*). The FTIR measurements were taken in the attenuated total reflectance (ATR) mode at a resolution of 4 cm^{-1}, as described previously (*52*). Briefly, FTIR spectra were recorded on a Thermo-Nicolet-6700 FT-IR spectrometer (Thermo Scientific) equipped with a liquid nitrogen-cooled MCT detector. The instrument was purged with ultrapure nitrogen for 1 h before the start of the experiment. The protofibrils formed when aggregation was induced by HFIP, TFE, or heat were concentrated ∼50-fold (final concentration of > 1 mM) using a centricon ultrafiltration device (Millipore) with a 3 kDa cutoff. For each sample, a buffer reading acquired under the same conditions was used as a blank; 512 interferograms were averaged for each sample. Water vapor correction was applied to remove any contribution from moisture in the FTIR spectra. To confirm that the process of concentration did not alter the nature of the protofibrils, DLS distributions of the concentrated FTIR samples were also determined. The DLS distribution did not change upon concentration of the samples (data not shown).

Disaggregation of the Protofibrils. Protein (20 μM) was aggregated in the presence of 10% HFIP. Upon completion of the aggregation reaction, the protein solution was diluted 10-fold into 50 mM Tris buffer such that the final protein and HFIP
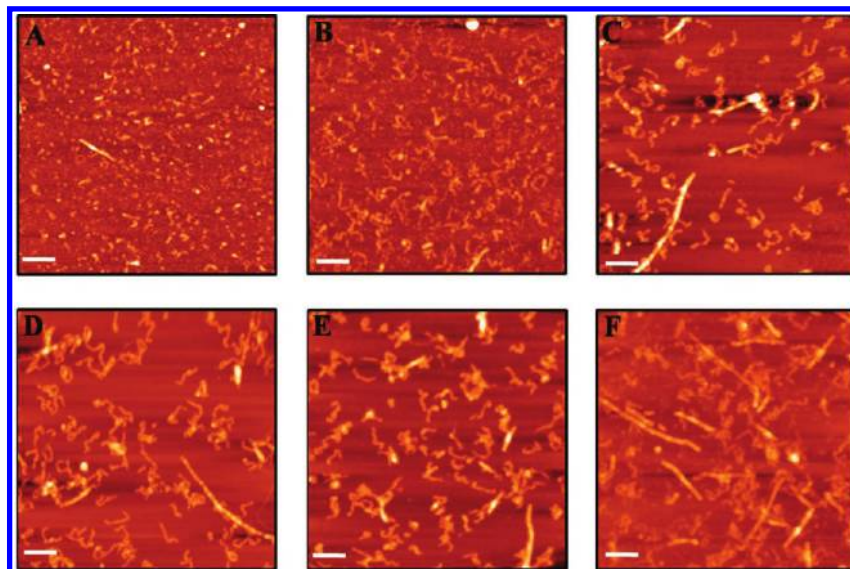
FIGURE 1: AFM images of aggregates formed at different time points of HFIP-induced aggregation of 25 μM protein. Each image represents a 1.5 μm × 1.5 μm scan. The different time points imaged were 10 min, 30 min, 1 h, 2 h, 2.6 h, and 23 h (A−F, respectively). The scale bars represent 200 nm.

concentrations were 2 μM and 1%, respectively, and the final pH was 8. For the study of the disaggregation of the TFE-induced protofibrils, the final protein and TFE concentrations used were 2 μM and 1%, respectively. The stability of the heat-induced protofibrils was studied at a final protein concentration of 2 μM. In addition, 1% HFIP was also included in the buffer at pH 8. The decrease in the ThT binding capacity of the solution was monitored by measurement of fluorescence on a Fluoromax-3 spectrofluorimeter (Jobin Yvon). The instrumental settings were the same as those used for the ThT binding assay.

Seeding Experiments. The seeding experiments were conducted with 5 μM protein. After incubation for 2 h at pH 2.7, HFIP was added to the protein solution to a final concentration of 10% (v/v). Immediately after HFIP addition, a calculated amount of the protein solution was discarded and replaced with a solution of seed so that the final protein concentration remained at 5 μM. The seed was comprised of a 5 μM protein solution that had been allowed to aggregate at pH 2.7 and 25 °C for 4.5 h in the presence of 10% HFIP.

Data Analysis. For each of the kinetic traces obtained with the various probes used, the fractional change at each time point was determined by using the following equation:

$$\text{fractional change} = \frac{S - S_{\text{initial}}}{S_{\text{final}} - S_{\text{initial}}} \quad (1)$$

where S represents the signal at time t, S_{initial} represents the signal at the first time point of aggregation, and S_{final} represents the signal at the end of the reaction.

The apparent rate constant of elongation was determined by fitting the data (excluding the initial 20% of signal change) to the single-exponential equation

$$S = S_0 + a(1 - e^{-t/\tau_{\text{el}}}) \quad (2)$$

where S_0 is the signal at time zero, a is the amplitude of the signal change, and τ_{el} is the time constant of elongation.

RESULTS

AFM Characterization of the HFIP-Induced Protofibril Formation Reaction. Protofibrils of barstar were formed by incubation of the A form at pH 2.7 in the presence of 10% HFIP

at 25 °C. At various time points during the reaction, a small aliquot was withdrawn and imaged on AFM mica. Figure 1 shows the AFM characterization of the structures formed at various time points of the HFIP-induced reaction. At 10 min, a large number of small spherical oligomers with average diameters (as determined from their Z heights in the AFM images) of 2.3 ± 0.5 nm, along with short straight fibrils with diameters of 8− 10 nm, are seen. At 30 min, short curly protofibrils are also seen to coexist with the spherical oligomers and fibrils. As the reaction progresses, the spherical oligomers disappear and longer protofibrils are seen. It appears that protofibril formation proceeds via the association of spherical oligomers. Interestingly, fibrils are seen to be present at all time points of the reaction investigated, even at early times where very few if any protofibrils can be observed.

HFIP-Induced Protofibrils Are Longer Than Heat-Induced Protofibrils. In the absence of HFIP, we formed protofibrils by conducting the aggregation reaction at 60 °C, a temperature at which aggregation is much faster than it is at 25 °C (*35*). Protofibrils formed in the aggregation reaction in the absence of any alcohol are therefore termed heat-induced protofibrils.

The comparison of the lengths of the protofibrils formed in the presence and absence of 10% HFIP is shown in Figure 2. It is seen that the average length of the HFIP-induced protofibrils (300 nm) is more than 3 times that of those formed in the absence of HFIP (90 nm). The length distributions of the protofibrils formed in the absence of HFIP are very similar to those of TFE-induced protofibrils (data not shown). Surprisingly, the distributions of lengths (Figure 2C) are not exponential (*69*). As one can see from the insets, the protofibrils formed under both conditions show a highly beaded appearance. The beaded nature is more prominent for the HFIP-induced protofibrils. Furthermore, the widths of the HFIP and heat-induced protofibrils were found to be very similar (∼19.0 ± 3.0 nm), when measured using the same cantilever. It should, however, be noted that it is not possible to obtain reliable estimates of the absolute widths of protofibrils from AFM measurements because of tip broadening artifacts associated with AFM cantilevers.

The comparison of heights of the protofibrils formed in the presence of 10% HFIP and 10% TFE is shown in Figure 3. The mean heights of the HFIP-induced protofibrils were found to be
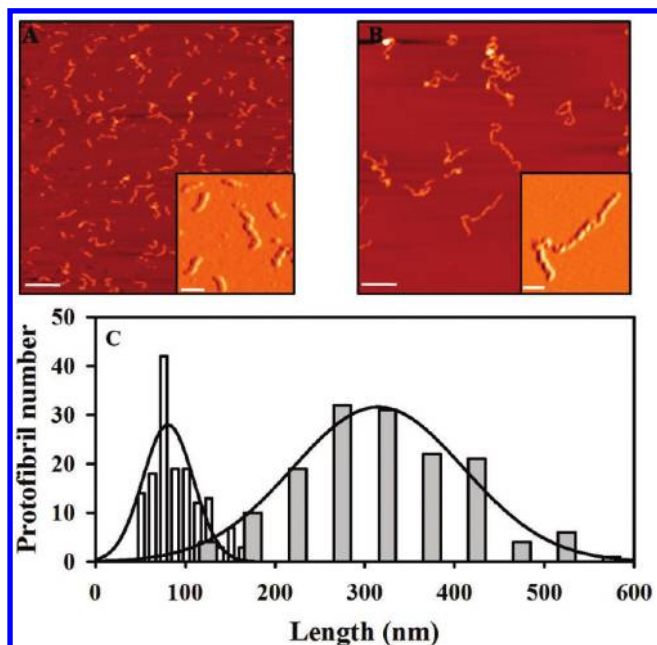
FIGURE 2: AFM images of heat-induced and HFIP-induced proto-fibrils formed by 25 μM barstar. Each image represents a 1.5 μm × 1.5 μm scan. (A) Heat-induced protofibrils formed after aggregation for 3.9 h. (B) HFIP-induced protofibrils formed after aggregation for 2.6 h. The scale bars represent 200 nm. The insets in panels A and B show magnified images of the same samples that demonstrate the beaded appearance of the protofibrils. Scale bars in the insets represent 60 nm. (C) Distributions of the lengths of the heat-induced protofibrils (white bars) and of the HFIP-induced protofibrils (gray bars). The solid lines represent Gaussian fits to the distributions.

2.4 ± 0.5 nm, while those of the TFE-induced protofibrils were found to be 1.3 ± 0.3 nm. The heights of the heat-induced protofibrils were found to be similar to those formed in the presence of HFIP (data not shown). Panels D and E of Figure 3 show conventional TEM images of the protofibrils formed in the presence of TFE and HFIP, respectively. The TEM images show that the widths of the TFE-induced protofibrils are significantly shorter than those of the HFIP-induced protofibrils, but the measured widths are expected not to be precise because of the deposition of uranyl acetate along the lengths of the protofibrils. In principle, it should be possible to confirm that HFIP-induced and TFE-induced protofibrils have different external dimensions, as seen by AFM, by conducting mass per length (MPL) analyses of the TEM data. MPL analysis using conventional TEM has been applied elegantly to differentiate between fibrils of different morphologies (*70*); however, protofibrils are much thinner than fibrils (see above), and the TFE-induced protofibrils in particular display a contrast that is too poor for such analysis (Figure 3D).

Structural Characterization of the Protofibrils Formed by Barstar under Different Conditions. The structural properties of protofibrils induced by 10% HFIP, by heat, and by 10% TFE were investigated using multiple probes. Figure 4A shows the far-UV CD spectra of the protofibrils formed under the three conditions, as well as that of the A form. The minima of the spectra for the HFIP- and TFE-induced protofibrils are red-shifted by ~3 nm compared to the minimum in the spectrum of the heat-induced protofibrils, and the ellipticity at 216 nm (θ_{216}) is significantly larger for the HFIP-induced protofibrils compared to that of the heat-induced and TFE-induced protofibrils. Because straight fibrils are also formed along with protofibrils in the presence of HFIP (Figure 1), it was necessary to demonstrate

that the CD spectrum of the HFIP-induced protofibrils was not different because of the coexistence of fibrils. The CD spectrum did not change significantly after the sample was spun at 14000 rpm for 45 min (data not shown), suggesting that only a small percentage of protein molecules formed fibrils under this condition. The secondary structure contents of the protofibrils were estimated by deconvolution of the spectra, and the results of the deconvolution are presented in the legend of Figure 4A. The HFIP-induced protofibrils appear to possess substantially more α-helical structure and substantially less β-sheet structure than both the heat- and TFE-induced protofibrils. The secondary structures of the heat-induced and TFE-induced protofibrils appear similar.

Fourier transform infrared spectroscopy was conducted in the attenuated total reflectance mode (ATR-FTIR). The solution ATR-FTIR spectra of the protofibrils formed under the three different conditions are shown in Figure 4B. Differences in the spectra are seen in the amide I (1600−1700 cm^{-1}) and amide II (1500−1600 cm^{-1}) regions. The two peaks of interest in the amide I region are at 1615−1636 cm^{-1}, which is indicative of the cross β-motif, and at 1650 cm^{-1}, which corresponds to α-helical segments or random coil structures (*71*). The amide I region of the HFIP-induced protofibrils shows two peaks, the major peak corresponding to the cross-β motif at 1620 cm^{-1} and a second smaller peak in the form of a shoulder at 1650 cm^{-1}. The FTIR spectrum of the heat-induced protofibrils is very similar to that of the HFIP-induced protofibrils. In contrast, the TFE-induced protofibrils exhibit predominantly only one peak in the amide I region at 1616 cm^{-1}. The HFIP- and TFE-induced protofibrils also differ in the peaks seen in the amide II region.

Figure 4C shows the DLS size distributions of the A form as well as of the protofibrils induced by HFIP, heat, and TFE. The A form has a narrow size distribution centered at 6 nm. The protofibrils formed under all three conditions are significantly larger. The size distributions of the TFE- and heat-induced protofibrils are similar, with peaks centered at 18−20 nm for both. The size distribution of the HFIP-induced protofibrils is, however, larger with a peak in the distribution at ~43 nm.

The stabilities of the protofibrils were assessed by monitoring the decrease in the magnitude of the thioflavin T (ThT) fluorescence signal, upon transfer of the protofibrils to pH 8. To ensure that the final disaggregation conditions were similar and that the stability of the protofibrils was not affected by the HFIP present in the solution upon the transfer to pH 8, the protofibrils formed in the presence and absence of alcohol were both disaggregated in the presence of 1% HFIP. The HFIP-induced protofibrils are the most stable: only ~28% of the initial fluorescence signal is lost at 21 h (Figure 4D). The heat-induced protofibrils possess inter-mediate stability: ~65% of the initial ThT fluorescence signal is lost at 21 h (Figure 3D).The TFE-induced protofibrils are the most unstable: ~80% of the initial signal is lost within the first 2 min of the disaggregation reaction (data not shown). The stability of the protofibrils formed in the absence of alcohol is only marginally reduced when they are disaggregated in the absence of HFIP (data not shown).

Kinetics of Formation of HFIP-Induced Protofibrils Monitored by ThT Fluorescence and Far-UV CD Measurements. The kinetics of the aggregation reaction in the presence of 10% HFIP was followed using multiple probes that report on different aspects of the aggregation process. Figure 5A shows the increase in ThT fluorescence of 25 μM protein with the progress of the aggregation reaction. ThT binds weakly to the A
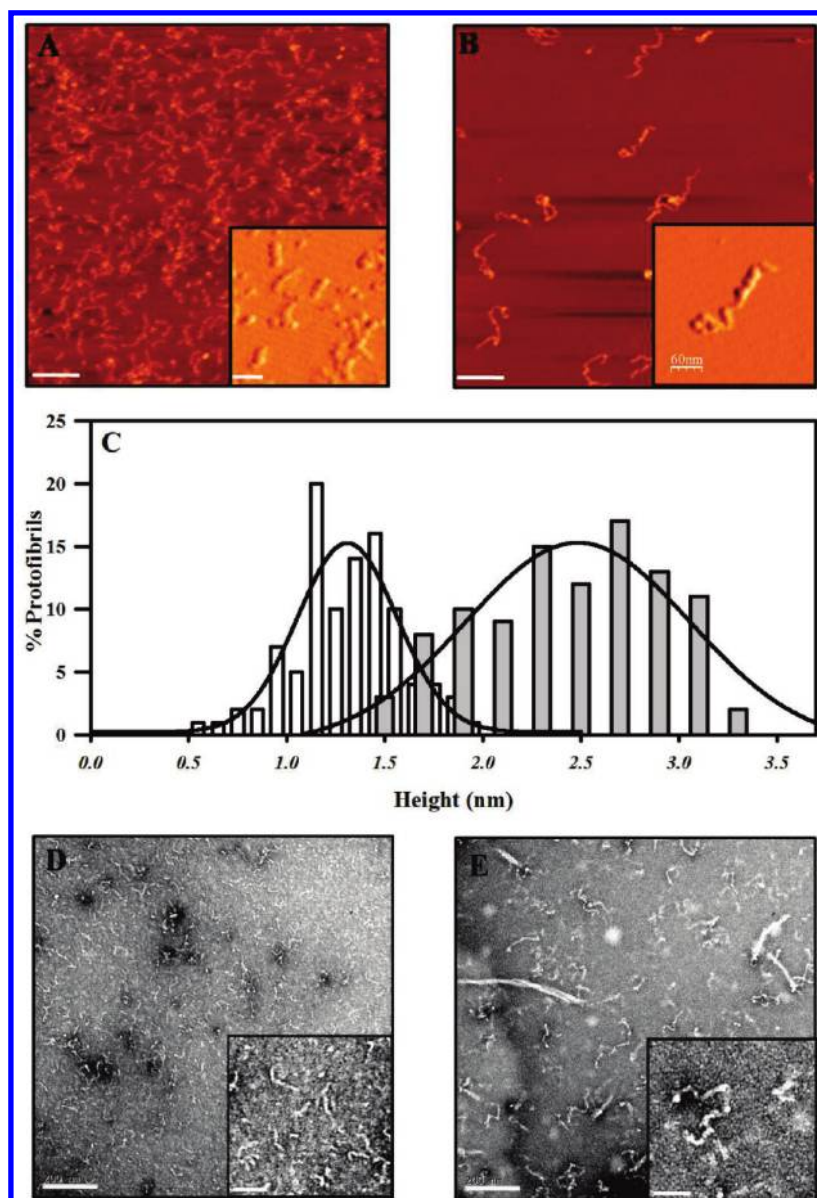
FIGURE 3: Structures of TFE-induced and HFIP-induced protofibrils formed by 25 μM barstar. Panel A is an AFM image of TFE-induced protofibrils formed after aggregation for 55 min. Panel B is an AFM image of HFIP-induced protofibrils formed after aggregation for 2.6 h. Each image represents a 1.5 μm × 1.5 μm scan, and the scale bar in each represents 200 nm. The insets in panels A and B show magnified images of the same sample that demonstrate the beaded nature of the protofibrils. The scale bars in the insets represent 60 nm. Panel C shows the distributions of the heights of the TFE-induced (white bars) and HFIP-induced protofibrils (gray bars). The solid lines represent Gaussian fits to the distributions. Panels D and E show TEM images of the protofibrils formed by 25 μM barstar in the presence of TFE and HFIP, respectively. The scale bars represent 200 nm. The insets in panels D and E show magnified TEM images of the samples. The scale bars in the insets represent 60 nm.

form and strongly to aggregated proteins and, hence, is used as a nonspecific probe to monitor conformational conversion during the aggregation process. There is an abrupt increase in the fluorescence immediately upon addition of HFIP to the A form. The subsequent kinetics fits well to a sigmoidal equation, but the lag phase is weak. The inset shows that a marginally more perceptible lag phase is seen for the aggregation of 5 μM protein. The HFIP-induced aggregation kinetics is highly reproducible, as is evident from the small error bars in the experiment. At all time points, the solution was found to be clear, indicating the absence of precipitates that could interfere with spectroscopic measurements such as CD.

It needs to be mentioned here that because protofibrils disaggregate under the conditions used in the ThT assay (pH 7.9), the ThT fluorescence signal decays both during the ~10 s mixing dead time of the ThT assay and during the subsequent 20 s of measurement. The extent of disaggregation that occurs during

these 30 s, as measured by the decrease in the ThT fluorescence, is marginal for fully formed protofibrils at the end of the reaction (Figure 4D) but is significant for the smaller aggregates (spherical oligomers and shorter protofibrils) present early in the reaction (data not shown). Consequently, the measured ThT fluorescence signal underestimates the true signal for assays conducted at early time points but not at late time points. The observed rate constant is therefore an underestimate of the true rate constant for the development of ThT binding sites. When the early aggregates are stabilized by the inclusion of higher concentrations (10%) of HFIP in the ThT assay solution (data not shown), the decrease in ThT fluorescence during the 30 s duration of the assay at each time point of aggregation is smaller, and the observed rate constant appears to be faster.

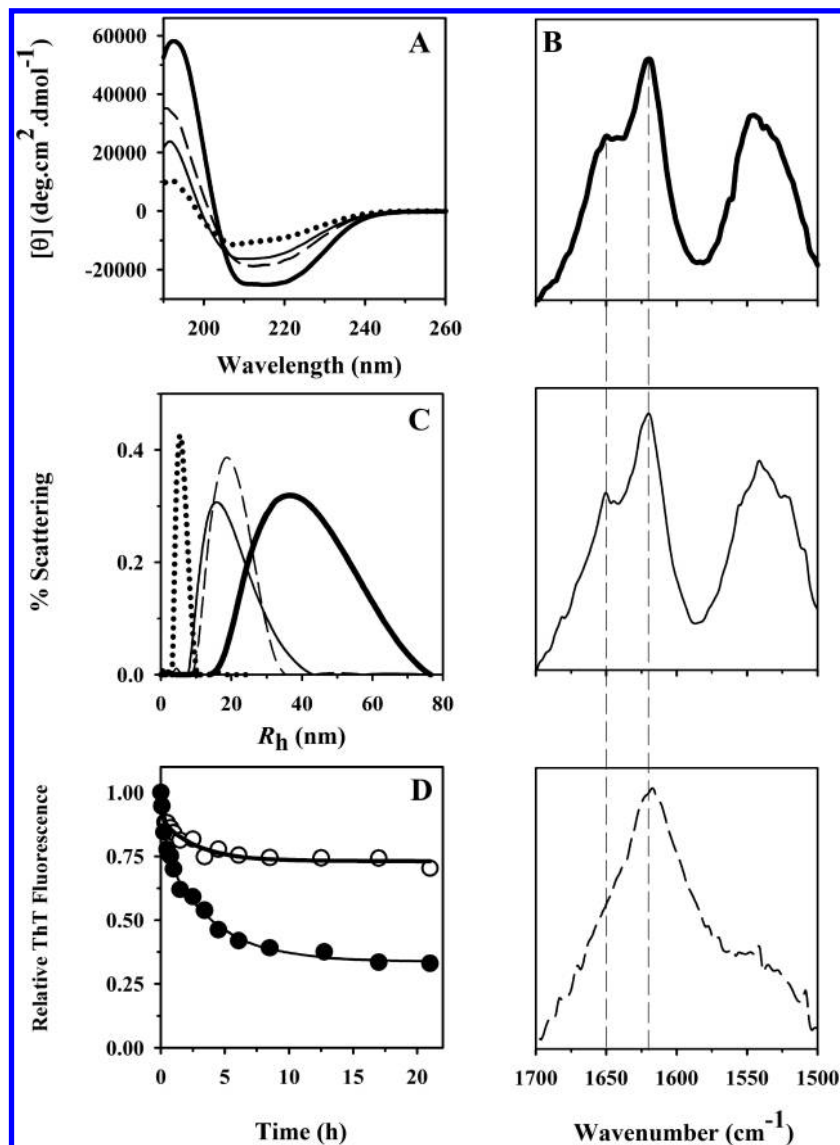Figure 5B shows far-UV CD spectra of 25 μM aggregating protein at different times of protofibril formation. After

FIGURE 4: Structural characterization of HFIP-induced, heat-induced, and TFE-induced protofibrils. Barstar (25 μM, pH 2.7) was allowed to aggregate from the A form in the presence of 10% HFIP at 25 °C, in the presence of 10% TFE at 25 °C, or in the absence of any added alcohol at 60 °C for a time $3/k$, where k is the apparent rate constant of elongation as determined from measurement of the far-UV CD kinetics. This time corresponds to 167 min for the HFIP-induced aggregation reaction, 55 min for the TFE-induced aggregation reaction, and 3.9 h for the heat-induced aggregation reaction. In all the panels, the dotted line represents the data for the A form, the thick solid line the data for the HFIP-induced protofibrils, the dashed line the data for the TFE-induced protofibrils, and the thin solid line the data for the heat-induced protofibrils. (A) Far-UV CD spectra of the protofibrils. The values for the mean residual ellipticity were calculated using the initial monomer concentration. Deconvolution of the CD spectra gave estimates of the percentages of α-helical structure, β-sheet structure, and random coil (which includes turns and unordered regions) of 23, 26, and 51% for the A form; 69, 8, and 23% for the HFIP-induced protofibrils; 36, 21, and 43% for the heat-induced protofibrils; and 43, 22, and 35% for the TFE-induced protofibrils, respectively. (B) FTIR spectra of the protofibrils formed under the three conditions. The lines drawn through the spectra at 1620 and 1650 cm^{-1} represent the positions expected for β-sheet-rich structures and α-helical/random coil structures, respectively. (C) DLS distributions. (D) Disaggregation kinetics of the HFIP-induced (O) and heat-induced (●) protofibrils at pH 8. The kinetic traces were obtained by monitoring the decrease in the ThT fluorescence upon the transfer to pH 8.

HFIP-induced aggregation for 2 min, the far-UV CD spectrum indicates that an intermediate form with high α-helical content has formed. Spectral deconvolution (see the legend of Figure 5B) indicates that during this first stage of HFIP-induced protofibril formation, the α-helical content has increased from 25% for the starting A form to 87% for the intermediate form, while the β-sheet content has decreased from 28 to 2%. Subsequently, in the second stage of aggregation, the intermediate form transforms into the final protofibrils, the β-sheet content increases from 2 to 8%, and the α-helical content appears to decrease from 87 to 69%. During the second stage of aggregation, the spectra change in shape with time of aggregation, but no isodichroic point is

seen, indicating that the transition occurs in a gradual manner, through a continuum of forms.

The far-UV CD signal at 216 nm (θ_{216}) as well as at 222 nm (θ_{222}) was used for studying the changes in secondary structure accompanying the HFIP-induced aggregation reaction of 25 μM protein. As expected from Figure 5B, during the first stage of HFIP-induced aggregation, θ_{216} (Figure 5C) and θ_{222} (data not shown) increase immediately upon addition of HFIP to the A form, indicating the formation of the intermediate form rich in α-helical content. Subsequently, in the second stage of the conformational change, both θ_{216} and θ_{222} (data not shown) decay gradually with identical apparent rate constants to ~80% of the
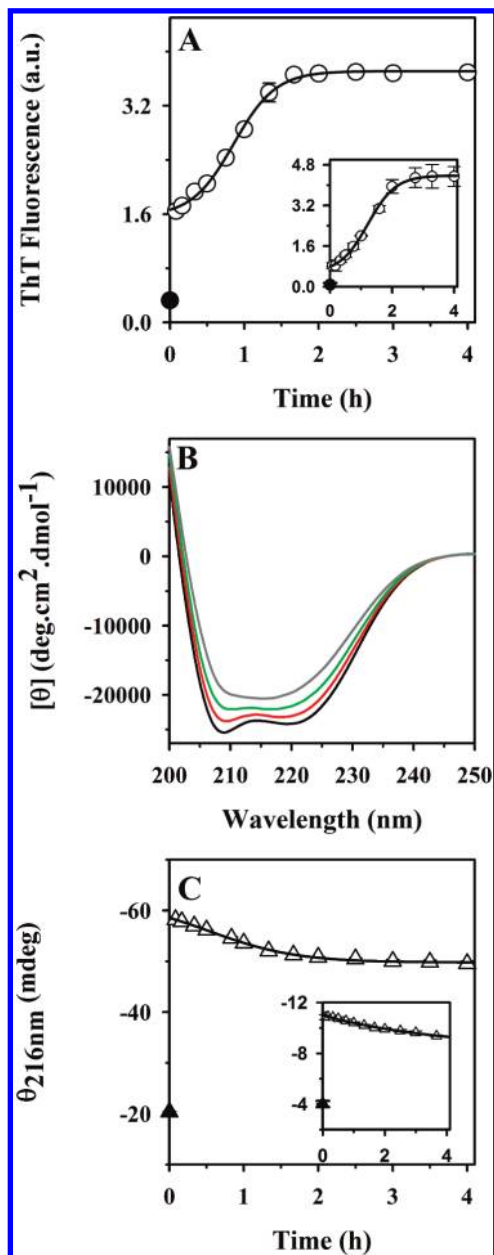
FIGURE 5: Kinetics of protofibril formation by barstar in 10% HFIP at 25 °C. (A) Kinetics of aggregation of 25 μM protein monitored by ThT fluorescence. The inset shows the kinetics of aggregation of 5 μM protein monitored by ThT fluorescence. (B) CD spectra at four different times during the aggregation of 25 μM protein: (black) 2 min, (red) 30 min, (green) 60 min, and (gray) 240 min after addition of HFIP. Deconvolution of a spectrum collected between 190 and 250 nm at 2 min after addition of HFIP (data not shown) gave levels of α-helical structure, β-sheet structure, and random coil (which includes turns and unordered regions) of 87, 2, and 11%, respectively. (C) Kinetics of aggregation of 25 μM protein monitored by far-UV CD at 216 nm (θ_{216}). The inset shwos the kinetics of aggregation of 5 μM protein monitored by θ_{216}. The error bars in panels A and C and their insets represent standard errors of the mean. Filled symbols at time zero indicate the signals of the A form. The solid lines through the data represent fits to a sigmoidal equation.

maximal value. The inset in Figure 5C shows that the observable kinetics of aggregation is slower for 5 μM protein, but the initial jump in the θ_{216} signal occurs to the same extent as it does for 25 μM protein.

Kinetics of Formation of HFIP-Induced Protofibrils As Determined by Dynamic Light Scattering. Dynamic light scattering (DLS) is a technique that measures the distribution of

sizes of particles (hydrodynamic radius) in a solution. Figure 6A shows the size distributions of the A form and the aggregates formed at five different points of time during the HFIP-induced aggregation reaction. The size distribution changes progressively from that of the A form with smaller values of the hydrodynamic radius and a narrow distribution to a broader one with larger values of the hydrodynamic radius.

Figure 6B demonstrates the aggregation kinetics of 25 μM protein as followed by a change in the scattering intensity (SI) over time. SI is proportional to both the size and the amount of aggregated material. The scattering intensity changes in a sigmoidal manner and shows a weak lag phase. Again, the lag phase is more pronounced for the aggregation reaction of 5 μM protein. Interestingly, while there is an initial jump in R_H, as there is in θ_{216} and ThT fluorescence, no initial jump in scattering intensity is seen at 5 and 25 μM protein. This suggests that only a small fraction of protein molecules initially form larger aggregates.

The change in the mean hydrodynamic radius (R_H) over the time course of the aggregation reaction of 25 μM protein in the presence of 10% HFIP is shown in Figure 6C. Immediately upon addition of HFIP, the A form is converted into a form with a higher R_H that then grows in size. It is seen that for 5 μM protein, the kinetics is clearly sigmoidal in nature (Figure 6C, inset), while for 25 μM protein, the sigmoidal nature of the kinetics is barely perceptible. The final R_H is greater for 5 μM protein than for 25 μM protein, suggesting that the protofibrils that form at the lower protein concentration should be longer. Surprisingly, however, AFM measurements revealed that the lengths of the protofibrils formed at both protein concentrations are not different (data not shown). The measured mean length of protofibrils formed by 25 μM protein is $\sim$300 nm (Figure 2), which predicts a value of $\sim$28 nm for the R_H (*72, 73*). In contrast, the measured R_H is $\sim$45 nm (Figure 6A). It appears, therefore, that the R_H distribution may be skewed to higher values of R_H because of the presence of minute amounts of fibrils (Figure 1), and that there is probably a difference in the amount and length of the fibrils formed at the different concentrations. This possibility has not been investigated as the fraction of protein molecules that form fibrils is very small, and it is therefore difficult to conduct length measurements with fibrils.

Structural Rearrangement As Monitored by Far-UV CD Is the Slowest Step in the HFIP-Induced Protofibril Reaction. Panels A and B of Figure 7 show the dependence on protein concentration of the rate constant of elongation of the HFIP-induced protofibril reaction, using the four different probes, namely, SI, ThT fluorescence, R_H, and θ_{216}. For each probe, the apparent rate constant of elongation at a particular protein concentration was obtained by fitting the fractional change in signal to a single-exponential equation after first excluding the initial $\sim$20% of the signal change. The rate constants monitored by R_H, SI, and ThT fluorescence are similar and are much faster than the rate constants monitored by far-UV CD at every concentration.

Features of a Classical Nucleation-Dependent Polymerization Reaction Are Absent in the HFIP-Induced Aggregation Reaction of Barstar. Classically, protein aggregation is known to follow sigmoidal kinetics when the aggregation process occurs in a nucleation-dependent manner. Because the kinetics followed by the different probes (except CD) is sigmoidal with a weak lag phase, plots of the log(rate of elongation) (log k) versus log(protein concentration) (log c) were obtained (insets, Figure 7A, B). The slopes were found to be < 1. For a nucleation-dependent
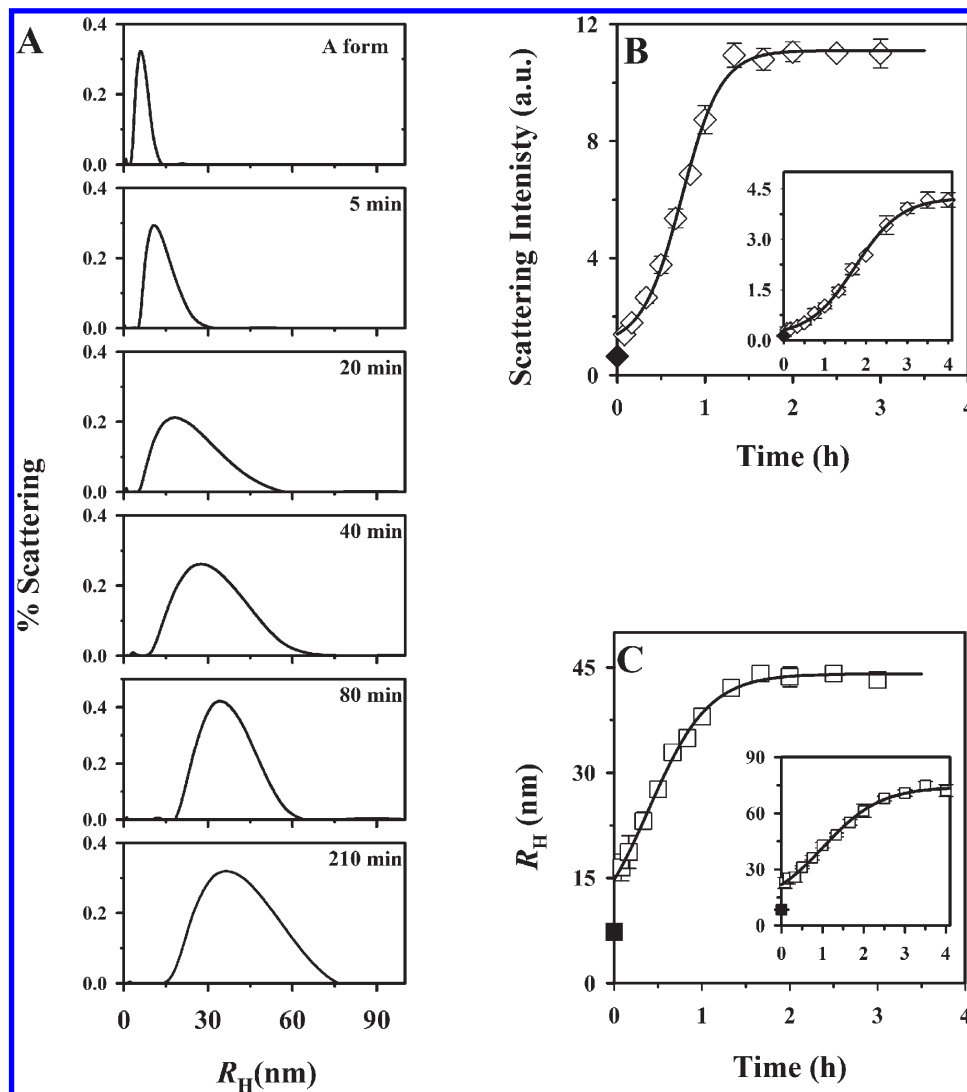
FIGURE 6: Kinetics of protofibril formation by barstar in 10% HFIP at 25 °C monitored by DLS. (A) DLS distributions of the A form and those at five different time points of aggregation (as indicated in the panels) of 25 μM protein. (B) Plot of scattering intensity vs time for the aggregation of 25 μM protein. The inset shows the scattering intensity vs time for 5 μM protein. (C) Change in R_H with time for the aggregation of 25 μM protein. The inset shows R_H vs time for the aggregation of 5 μM protein. In panels B and C, the filled symbols at time zero represent the signals for the A form.

polymerization reaction, the slope of the log k versus log c plot equals $(n^* + 1)/2$, where n^* is the size of the nucleus (*74*).

The plots of the amplitude of the signal change (as measured by the final signals) versus protein concentration obtained from the ThT fluorescence data, SI data, and CD data are shown in Figure 7C. The three probes all show similar dependencies of their change in their amplitude on protein concentration, and the straight line fit through the data passes through the origin, once again indicating the absence of any critical concentration for the reaction.

Figure 7D and its inset demonstrate the dependence of the lag times on protein concentration using the various probes. The lag times were determined by extrapolation of the single-exponential fits obtained from each of the kinetic traces (after removal of the initial 20% of the signal) to the time at which the change in signal being monitored by the probe under consideration was zero. For the four different probes used in this study, the lag time was found to decrease with an increase in protein concentration, but in a very weak manner.

Effect of Seeding on Protofibril Formation by Barstar in the Presence of 10% HFIP. One of the hallmarks of a

nucleation-dependent reaction is that the reaction is accelerated in the presence of a small amount of preformed aggregate (seed). This occurs because the initial nucleation event is unfavorable and is bypassed by seeding. Figure 8 shows the effect of seeding on the kinetics of HFIP-induced protofibril formation of 5 μM barstar as monitored by the change in ThT fluorescence. The seed concentrations used were 10 and 20% (v/v). The observed elongation rate constant was found to be 1.1 ± 0.1 h^{-1} both in the presence and in the absence of the seed. The inset in the figure shows that the lag time decreases only modestly with increasing seed concentrations, and that the lag phase is not completely abolished even upon addition of 20% seed.

DISCUSSION

Alcohols and, in particular, fluorine-substituted alcohols such as HFIP and TFE have been used extensively to study protein aggregation (*62, 75−78*). Fluoroalcohols destabilize the native states of proteins and allow the formation of partially unstructured forms in the case of folded proteins and partially folded forms in the case of unstructured proteins (*59*). The effect of HFIP in destabilizing the native state is greater than that of other
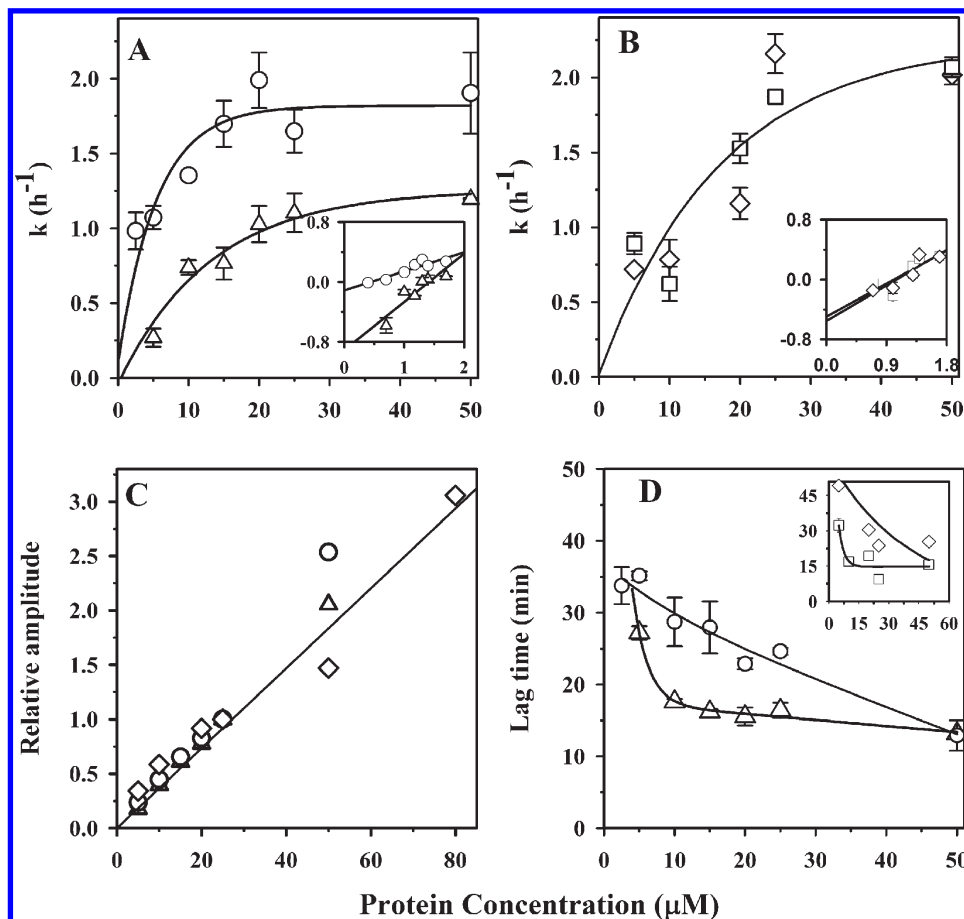
FIGURE 7: Dependence of the kinetics of HFIP-induced protofibril formation on protein concentration: (○) ThT fluorescence, (△) CD at 216 nm (θ_{216}), (◇) SI, and (□) R_H. (A) Dependence on protein concentration (c) of the observed rate constants of elongation (k) obtained using both ThT fluorescence and θ_{216} as probes. The inset contains plots of log k vs log c for both probes. The slope of the line was found to be 0.5. (B) Dependence of k obtained using SI and R_H data. The inset shows log k vs log c for both probes. (C) Relative amplitude vs protein concentration for the ThT fluorescence, SI, and CD. In each case, the data were normalized to a value of 1 for the amplitude seen for 25 μM protein. (D) Dependence of the lag time of the reactions monitored by ThT fluorescence and CD on protein concentration. The inset shows the dependence of the lag time of the SI and R_H data on the protein concentration. The lines in the main panels A−D are lines of inspection.
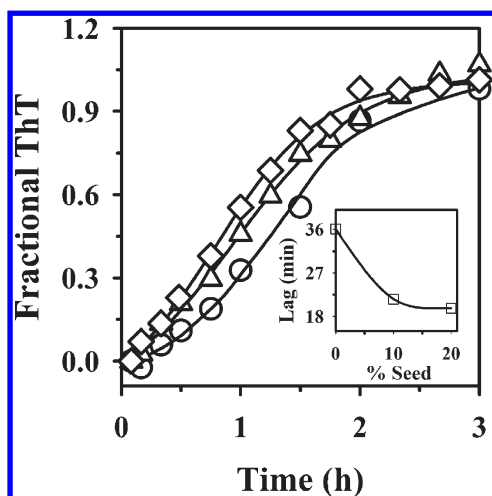

FIGURE 8: Effect of seeding on the aggregation kinetics of 5 μM barstar in the presence of 10% HFIP. Aggregation kinetics of 5 μM protein monitored by ThT fluorescence in the absence (○) and presence of either 10% seed (△) or 20% seed (◇). The inset shows the variation in lag times of aggregation with increasing seed concentration. The seed was comprised of a solution of 5 μM barstar that had been aggregated in the presence of 10% HFIP for 4.5 h.

alcohols because of a combination of factors like the dielectric constant, the hydrophobicity of side chains, the low polarity,

and its ability to self-associate (*79*). It has been shown for β2 microglobulin that the aggregation kinetics has a bell-shaped dependence on HFIP concentration (*62*). This dependence arises from the dual effects of HFIP on the hydrophobic and polar interactions necessary to maintain aggregate stability. Very high concentrations of HFIP induce a high α-helical content in proteins because of increased solvent hydrophobicity and prevent their aggregation (*59, 64*). However, at moderate concentrations, it is thought to promote aggregation by maintaining a critical balance between hydrophobic and polar interactions needed to form and maintain the cross β-structure seen in fibrils. HFIP might mediate its effect on the aggregation of proteins in two ways. It could preferentially bind to the polypeptide backbone, and this binding could effect conformational change in the protein (*60*). Alternatively, its ability to form clusters in aqueous solution, above a critical concentration of 10% (*60*), could enhance its ability to stabilize secondary structure in proteins, presumably by reducing the accessibility of the polypeptide backbone to water, which has been suggested (*62*).

In this study, the mechanism of protofibril formation by barstar in the presence of 10% HFIP has been investigated. The reaction shows several interesting features and leads to the formation of protofibrils that are markedly different in their structure and stability as compared to protofibrils of barstar formed under other conditions.

Structure of HFIP-Induced Protofibrils. The protofibrils formed in the presence of 10% HFIP are found to have average heights of ∼2.4 nm, indicating that they are composed of β-sheet bilayers. In this regard, they are very similar to the protofibrils of barstar formed in the absence of any alcohol. In contrast, the height of the protofibrils formed by barstar in the presence of TFE, another fluoroalcohol, is only ∼1.3 nm, indicating that the protofibrils consist of a monolayer of β-sheets (*52*). Furthermore, the HFIP-induced protofibrils show a more prominent beaded appearance as compared to heat or TFE-induced protofibrils (Figure 2).

In another study in which the effects of the two alcohols were studied, it was seen that fibrils formed by the K3 peptide of $\beta 2$ microglobulin in the presence of 10% HFIP were more heterogeneous and were composed of protofilaments that were laterally associated, thereby showing heights on AFM mica larger than the heights of those formed in the presence of 20% TFE (*62*). In the presence of 20% TFE, the fibrils formed were comprised mainly of single protofilaments that did not associate laterally. Because it is known that 10% HFIP is more effective than 10% TFE in inducing aggregation, a comparison was made of the protofibrils of barstar formed in the presence of 10% HFIP with those formed in the presence of 20% TFE. However, even in the presence of 20% TFE, the protofibrils formed by barstar are as thin as those formed in the presence of 10% TFE, with average heights of ∼1.3 nm (data not shown).

Polymer length depends on the binding constant with which polymerizing units add on to each other. The observation that the protofibrils formed in the presence of HFIP are much longer (300 nm) than those formed in the absence of the alcohol (90 nm) suggests that in the presence of HFIP, the binding constant is larger. The larger binding constant may be due to the alcohol causing a reduction in the level of polar interactions of the individual protein molecules with water, and a local environment with a reduced dielectric constant (*63*).

Both the CD and the FTIR spectra (Figure 4) indicate that the α-helical and β-sheet contents of the HFIP-induced protofibrils are different from those of TFE-induced protofibrils. The CD analysis indicates that the HFIP-induced protofibrils possess more α-helical structure and less β-sheet structure than the TFE-induced protofibrils. The FTIR spectrum of the HFIP-induced protofibrils does indeed indicate that both α-helical and β-sheet structures are present. On the other hand, the FTIR spectrum of the TFE-induced protofibrils indicates qualitatively that they are comprised mainly of β-sheet-rich structures and contain little contribution if any from other structural elements even though the CD spectrum indicates that substantial α-helical structure is present. At present, the reason for this discrepancy between the CD and FTIR data is not known, but the observation suggests that great care must be taken in the estimation of secondary structure by these two techniques. Nevertheless, both the CD and FTIR spectra indicate that the secondary structure contents of the HFIP-induced and TFE-induced protofibrils differ significantly in their proportions of β-sheet structure to other secondary structure. The DLS distributions of the HFIP-induced protofibrils are also much broader than the TFE-induced ones, indicating that they are comprised of a more heterogeneous population.

Mechanism of Formation of HFIP-Induced Protofibrils. The observation that the spherical oligomers formed early during aggregation disappear gradually over time, along with the formation of beaded protofibrils, suggests that the spherical oligomers self-associate and give rise to protofibrils (Figure 1).

In this regard, protofibril formation seems to follow an isodesmic polymerization mechanism (*37, 80*), with the spherical oligomers serving as the polymerizing units. This observation is further corroborated by the DLS data that show a progressive increase in the size of the aggregating species with time.

Interestingly, at all time points of the HFIP-induced reaction, straight fibrils with characteristic heights of 8−10 nm are observed. Such fibrils have not been observed in the aggregation reactions induced by heat or 10% TFE, where protofibrils are the main aggregates formed, along with higher-order spherical oligomers (*35, 50, 52*). At early time points of the HFIP reaction, the fibrils are short and they increase in length as the reaction progresses. Protofibrils and fibrils are both seen to be present at later times in the aggregation reaction. In future work, it will be important to determine the mechanism of formation of the fibrils and whether the protofibrils are off-pathway or on-pathway intermediates in the fibril formation reaction or whether the two species form on parallel pathways. For several other proteins, it has been suggested that fibrils form directly from protofibrils (*81, 82*), even though direct kinetic evidence has been lacking.

The kinetics of the HFIP-induced reaction as monitored by probes such as ThT fluorescence and SI is sigmoidal and shows a weak lag phase that is suggestive of a nucleation-dependent polymerization (NDP) reaction (*74, 83, 84*). It is possible that protofibrils might nucleate by the conformational change occurring either in the A form or in the larger spherical oligomers seen early during aggregation (Figure 1), and indeed, conformational conversion in larger spherical oligomers has been observed during the course of heat-induced protofibril formation by some mutant forms of barstar (*50*). Several observations are, however, inconsistent with an NDP mechanism. (a) There is no critical concentration barrier for the reaction (Figure 7C). (b) The lag phase observed has a very weak dependence on protein concentration (Figure 7D). (c) The addition of a seed does not abolish the lag phase (Figure 8). All these observations indicate that the mechanism is not nucleation-dependent but has salient features of an isodesmic polymerization reaction.

Structural Events during HFIP-Induced Aggregation. Immediately upon the addition of HFIP to the A form, the A form undergoes a rapid conformational change and forms an aggregate richer in α-helical content ($A_H\alpha$ form) as compared to the A form. Far-UV CD spectra of the aggregates formed after addition of different concentrations of HFIP to the A form for 1 min did not show any isodichroic point (data not shown). Furthermore, the fractional burst in the θ_{216} kinetics is the same at all protein concentrations during this first stage of protofibril formation. Both these observations suggest that all protein molecules are converted to the $A_H\alpha$ form. Thus, in the presence of 10% HFIP, it is likely that protofibril formation commences directly from the $A_H\alpha$ form, while in its absence, it commences directly from the A form (*35*).

Protofibril formation in the presence of 10% TFE also commences from a form rich in α-helical content ($A_T\alpha$). This form shows, however, significant differences from $A_H\alpha$. Deconvolution of the CD spectra of $A_H\alpha$ (Figure 5, legend) and $A_T\alpha$ (data not shown) indicates much greater helical content in the former and a much greater β-sheet content in the latter. The observation that $A_H\alpha$ shows significant ThT binding as compared to $A_T\alpha$ might appear surprising because ThT has been thought to bind nonspecifically to amyloid protofibrils and fibrils, and the extent of binding and the consequent fluorescence
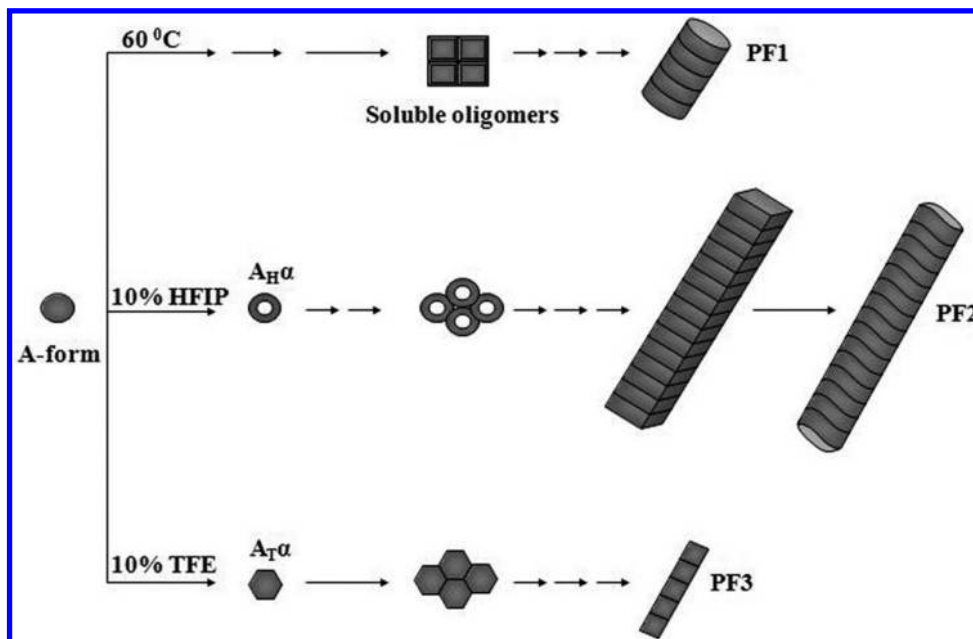
FIGURE 9: Pathways of protofibril formation by barstar. In the absence of any added alcohol, the A form converts directly into higher-order oligomeric intermediates, which elongate and undergo conformational conversion to form protofibrils PF1. In the presence of HFIP or TFE, protofibril formation occurs in two stages. In the first stage, α-helix-rich oligomeric intermediates ($A_H\alpha$ or $A_T\alpha$) are formed. In the second stage, these elongate and undergo conformational conversion to form protofibrils PF2 (HFIP) or PF3 (TFE). In the case of the HFIP-induced reaction, conformational conversion during the second stage of protofibril formation occurs in two sequential steps, while for TFE-induced protofibrils, it seems to occur in a single step. The protofibrils formed under all three conditions differ in their internal structures. The lengths of the protofibrils induced by heat and TFE are similar and are ∼3 times shorter than the length of the HFIP-induced protofibrils. The HFIP- and heat-induced protofibrils have similar heights (∼2.4 nm), which are significantly greater than that of the TFE-induced protofibrils (∼1.3 nm).

change have been thought to reflect the extent of β-structure present. Very recently, it has, however, been reported that ThT binds only to specific motifs of β-structure in amyloid aggregates, which are rich in aromatic amino acid residues (85−87). Hence, the binding of ThT and the consequent increase in its fluorescence are not correlated with the total amount of β-structure present. At present, the reason why $A_H\alpha$ binds ThT more than does $A_T\alpha$ is not known, but the observation that the aggregation reactions in the presence of the two fluoroalcohols commence from intermediate forms that both possess significant α-helical secondary structure is not unique. In the case of α-synuclein, too, α-helical intermediates formed at low fluoroalcohol concentrations have been shown to act as precursors to aggregation (59).

Transformation of $A_H\alpha$ to Protofibrils. $A_H\alpha$ gradually transforms into protofibrils, and this transformation is accompanied by an increase in β-sheet structure content and a reduction in α-helical structure content. This structural transition occurs in a gradual manner (Figure 5B) as does the growth of the aggregates. In contrast to the transformation of $A_H\alpha$ to protofibrils that is accompanied by a decrease in ellipticity (Figure 5C), the gradual transformation of the $A_T\alpha$ form into β-sheet-rich protofibrils was seen to be accompanied by an increase in ellipticity (52).

The transformation of $A_H\alpha$ into protofibrils during the second stage of protofibril formation occurs in at least two kinetic steps, because the observed rate constant for the transformation is significantly slower when measured by the change in θ_{216} than when measured by the change in either ThT fluorescence, SI, or R_H. Hence, it appears that the conformational conversion of the α-helix-rich $A_H\alpha$ to the protofibrils occurs in two steps. In the first step, additional ThT binding sites are created as the aggregate grows in size. In the second slower step, α-helical structure is

lost and β-sheet structure is formed. The probes sensitive to the first step, namely, ThT fluorescence, SI, and R_H, show distinctly sigmoidal kinetics that arises as oligomers add linearly to the growing protofibrils in multiple sequential steps (52). The probe sensitive to the second step shows kinetics that can be adequately described as exponential. The absence of a lag phase in the CD-monitored kinetics suggests that the major fraction of the conformational conversion occurs late during protofibril formation but that a minor fraction of the change occurs early during the transformation of $A_H\alpha$ to protofibrils. The observation that the apparent rate constant saturates in value at high protein concentrations is indicative of the conformational conversion step becoming rate-limiting at high protein concentrations.

For many proteins, it has been observed that conformational conversion as marked by ThT binding as well as by changes in the secondary structure occurs concomitantly (88, 89). The same holds true for protofibrils of barstar induced by TFE or heat, where it is observed that the ThT- and θ_{216}-monitored kinetics appear to be similar (35, 50, 52). This study is one of the first to delineate two steps in conformational conversion from the initially formed α-helix-rich oligomeric intermediate, by showing that the change in the CD spectrum occurs slower than the change in ThT binding.

Heterogeneity of Protofibril Structures and Pathways. In this study, the pathway of protofibril formation in the presence 10% HFIP has been characterized. There are some important similarities and differences between this pathway and the ones seen to operate in the absence of any alcohol, or in the presence of the related alcohol, TFE (Figure 9).

Importantly, it is seen that the aggregation reaction in the presence of alcohols is greatly accelerated as compared to that in the absence of alcohol. This suggests that these fluoroalcohols are

very effective in mediating the balance of polar and hydrophobic interactions that greatly aid the aggregation process. Both the HFIP- and TFE-induced reactions show sigmoidal kinetics with a weak lag phase. However, the α-helical precursor is different in the two cases ($A_H\alpha$ vs $A_T\alpha$). For both reactions, the mechanism lacks the features of a NDP reaction and has some salient features of an isodesmic polymerization reaction.

In the absence of HFIP, aggregation is found to commence directly from the A form and occurs with exponential kinetics and through a gradual association of higher-order oligomeric intermediates. Conformational conversion in the HFIP reaction occurs in two distinct steps, while both steps occur concomitantly in the presence of heat or TFE (Figure 9).

In summary, the protofibrils formed by barstar are extremely heterogeneous and the structures they form depend on, and are very sensitive to, the aggregation conditions. While both in the presence and in the absence of HFIP, protofibrils comprising a bilayer of β-sheets are formed, the presence of HFIP results in the formation of much longer protofibrils. In contrast, the protofibrils formed in the presence of the highly related fluoroalcohol TFE appear to be comprised mainly of β-sheet monolayers (*52*). The stability of the protofibrils formed is also strongly dependent on the aggregation conditions. The pathways utilized for the formation of protofibrils are also different and depend again on the aggregation condition (Figure 9). Work done with other proteins such as Aβ and α-synuclein has also demonstrated that fibril morphology is strongly dependent on solution conditions (*13*, *14*, *40*, *78*).

The results of this study indicate that protofibril formation and stability are very strongly governed by a delicate balance between hydrophobic interactions that enhance intermolecular interactions and favor association of protein molecules and hydrogen bonding interactions that stabilize the overall β-sheet. The relative balance of these interactions is slightly different in the absence of any alcohol, in the presence of HFIP, and in the presence of TFE. It is quite remarkable that the two fluoroalcohols affect the aggregation pathway of barstar in fundamentally different ways such that the final protofibrils have distinct structures. It is possible that this difference arises because HFIP, unlike TFE, can preferentially bind to proteins through hydrophobic interactions (*60*). The results of this study suggest that the energy landscape for protofibril formation is rugged with many small energy traps, and that a minor perturbation in solvent conditions can alter the stability and structure of the end products drastically. This result has implications for future studies targeted toward guiding protofibril formation along pathways that might result in unstable and relatively less toxic structures.

REFERENCES

1. Mitchison, T., and Kirschner, M. (1984) Dynamic instability of microtubule growth. *Nature 312*, 237–242.

2. Selkoe, D. J. (2003) Folding proteins in fatal ways. *Nature 426*, 900–904.

3. Ross, C. A., and Poirier, M. A. (2004) Protein aggregation and neurodegenerative disease. *Nat. Med. 10* (Suppl.), S10–S17.

4. Fink, A. L. (1998) Protein aggregation: Folding aggregates, inclusion bodies and amyloid. *Folding Des. 3*, R9–R23.

5. Allison, A. C. (1973) The role of microfilaments and microtubules in cell movement, endocytosis and exocytosis. *Ciba Found. Symp. 14*, 109–148.

6. Jesior, J. C., Miller, A., and Berthet-Colominas, C. (1980) Crystalline three-dimensional packing is a general characteristic of type I collagen fibrils. *FEBS Lett. 113*, 238–240.

7. Chimon, S., Shaibat, M. A., Jones, C. R., Calero, D. C., Aizezi, B., and Ishii, Y. (2007) Evidence of fibril-like β-sheet structures in a neurotoxic amyloid intermediate of Alzheimer's β-amyloid. *Nat. Struct. Mol. Biol. 14*, 1157–1164.

8. Kunda, P., and Baum, B. (2009) The actin cytoskeleton in spindle assembly and positioning. *Trends Cell Biol. 19*, 174–179.

9. Brummel, K. E., Butenas, S., and Mann, K. G. (1999) An integrated study of fibrinogen during blood coagulation. *J. Biol. Chem. 274*, 22862–22870.

10. Lashuel, H. A., Petre, B. M., Wall, J., Simon, M., Nowak, R. J., Walz, T., and Lansbury, P. T., Jr. (2002) α-Synuclein, especially the Parkinson's disease-associated mutants, forms pore-like annular and tubular protofibrils. *J. Mol. Biol. 322*, 1089–1102.

11. Lashuel, H. A., Hartley, D. M., Petre, B. M., Wall, J. S., Simon, M. N., Walz, T., and Lansbury, P. T., Jr. (2003) Mixtures of wild-type and a pathogenic (E22G) form of Aβ40 in vitro accumulate protofibrils, including amyloid pores. *J. Mol. Biol. 332*, 795–808.

12. Kad, N. M., Thomson, N. H., Smith, D. P., Smith, D. A., and Radford, S. E. (2001) β₂-Microglobulin and its deamidated variant, N17D, form amyloid fibrils with a range of morphologies in vitro. *J. Mol. Biol. 313*, 559–571.

13. Hoyer, W., Antony, T., Cherny, D., Heim, G., Jovin, T. M., and Subramaniam, V. (2002) Dependence of α-synuclein aggregate morphology on solution conditions. *J. Mol. Biol. 322*, 383–393.

14. Malisauskas, M., Zamotin, V., Jass, J., Noppe, W., Dobson, C. M., and Morozova-Roche, L. A. (2003) Amyloid protofilaments from the calcium-binding protein equine lysozyme: Formation of ring and linear structures depends on pH and metal ion concentration. *J. Mol. Biol. 330*, 879–890.

15. Sawaya, M. R., Sambashivan, S., Nelson, R., Ivanova, M. I., Sievers, S. A., Apostol, M. I., Thompson, M. J., Balbirnie, M., Wiltzius, J. J., McFarlane, H. T., Madsen, A. O., Riekel, C., and Eisenberg, D. (2007) Atomic structures of amyloid cross-β spines reveal varied steric zippers. *Nature 447*, 453–457.

16. Chiti, F., and Dobson, C. M. (2006) Protein misfolding, functional amyloid, and human disease. *Annu. Rev. Biochem. 75*, 333–366.

17. Nelson, R., Sawaya, M. R., Balbirnie, M., Madsen, A. O., Riekel, C., Grothe, R., and Eisenberg, D. (2005) Structure of the cross-β spine of amyloid-like fibrils. *Nature 435*, 773–778.

18. Jonas, K., Tomenius, H., Kader, A., Normark, S., Romling, U., Belova, L. M., and Melefors, O. (2007) Roles of curli, cellulose and BapA in *Salmonella* biofilm morphology studied by atomic force microscopy. *BMC Microbiol. 7*, 70.

19. Kenney, J. M., Knight, D., Wise, M. J., and Vollrath, F. (2002) Amyloidogenic nature of spider silk. *Eur. J. Biochem. 269*, 4159–4163.

20. Fowler, D. M., Koulov, A. V., Alory-Jost, C., Marks, M. S., Balch, W. E., and Kelly, J. W. (2006) Functional amyloid formation within mammalian tissue. *PLoS Biol. 4*, e6.

21. Gregersen, N., Bross, P., Vang, S., and Christensen, J. H. (2006) Protein misfolding and human disease. *Annu. Rev. Genomics Hum. Genet. 7*, 103–124.

22. Soto, C., and Castilla, J. (2004) The controversial protein-only hypothesis of prion propagation. *Nat. Med. 10* (Suppl.), S63–S67.

23. Edskes, H. K., and Wickner, R. B. (2004) Transmissible spongiform encephalopathies: Prion proof in progress. *Nature 430*, 977–979.

24. Collinge, J. (2001) Prion diseases of humans and animals: Their causes and molecular basis. *Annu. Rev. Neurosci. 24*, 519–550.

25. Harper, J. D., and Lansbury, P. T., Jr. (1997) Models of amyloid seeding in Alzheimer's disease and scrapie: Mechanistic truths and physiological consequences of the time-dependent solubility of amyloid proteins. *Annu. Rev. Biochem. 66*, 385–407.

26. Shankar, G. M., Li, S., Mehta, T. H., Garcia-Munoz, A., Shepardson, N. E., Smith, I., Brett, F. M., Farrell, M. A., Rowan, M. J., Lemere, C. A., Regan, C. M., Walsh, D. M., Sabatini, B. L., and Selkoe, D. J. (2008) Amyloid-β protein dimers isolated directly from Alzheimer's brains impair synaptic plasticity and memory. *Nat. Med. 14*, 837–842.

27. Heise, H., Hoyer, W., Becker, S., Andronesi, O. C., Riedel, D., and Baldus, M. (2005) Molecular-level secondary structure, polymorphism, and dynamics of full-length α-synuclein fibrils studied by solid-state NMR. *Proc. Natl. Acad. Sci. U.S.A. 102*, 15871–15876.

28. Goldsbury, C., and Green, J. (2005) Time-lapse atomic force microscopy in the characterization of amyloid-like fibril assembly and oligomeric intermediates. *Methods Mol. Biol. 299*, 103–128.

29. Serpell, L. C., Sunde, M., Benson, M. D., Tennent, G. A., Pepys, M. B., and Fraser, P. E. (2000) The protofilament substructure of amyloid fibrils. *J. Mol. Biol. 300*, 1033–1039.

30. Sunde, M., Serpell, L. C., Bartlam, M., Fraser, P. E., Pepys, M. B., and Blake, C. C. (1997) Common core structure of amyloid fibrils by synchrotron X-ray diffraction. *J. Mol. Biol. 273*, 729–739.

31. Petkova, A. T., Ishii, Y., Balbach, J. J., Antzutkin, O. N., Leapman, R. D., Delaglio, F., and Tycko, R. (2002) A structural model for Alzheimer's β-amyloid fibrils based on experimental constraints from solid state NMR. *Proc. Natl. Acad. Sci. U.S.A. 99*, 16742–16747.

32. Sunde, M., and Blake, C. (1997) The structure of amyloid fibrils by electron microscopy and X-ray diffraction. *Adv. Protein Chem. 50*, 123–159.

33. Ignatova, Z., and Gierasch, L. M. (2005) Aggregation of a slow-folding mutant of a β-clam protein proceeds through a monomeric nucleus. *Biochemistry 44*, 7266–7274.

34. Kaylor, J., Bodner, N., Edridge, S., Yamin, G., Hong, D. P., and Fink, A. L. (2005) Characterization of oligomeric intermediates in α-synuclein fibrillation: FRET studies of Y125W/Y133F/Y136F α-synuclein. *J. Mol. Biol. 353*, 357–372.

35. Kumar, S., Mohanty, S. K., and Udgaonkar, J. B. (2007) Mechanism of formation of amyloid protofibrils of barstar from soluble oligomers: Evidence for multiple steps and lateral association coupled to conformational conversion. *J. Mol. Biol. 367*, 1186–1204.

36. Jain, S., and Udgaonkar, J. B. (2008) Evidence for stepwise formation of amyloid fibrils by the mouse prion protein. *J. Mol. Biol. 382*, 1228–1241.

37. Kumar, S., and Udgaonkar, J. B. (2010) Mechanisms of amyloid fibril formation by proteins. *Curr. Sci. 98*, 639–656.

38. Volles, M. J., and Lansbury, P. T., Jr. (2003) Zeroing in on the pathogenic form of α-synuclein and its mechanism of neurotoxicity in Parkinson's disease. *Biochemistry 42*, 7871–7878.

39. Goldsbury, C., Frey, P., Olivieri, V., Aebi, U., and Muller, S. A. (2005) Multiple assembly pathways underlie amyloid-β fibril polymorphisms. *J. Mol. Biol. 352*, 282–298.

40. Gosal, W. S., Morten, I. J., Hewitt, E. W., Smith, D. A., Thomson, N. H., and Radford, S. E. (2005) Competing pathways determine fibril morphology in the self-assembly of β2-microglobulin into amyloid. *J. Mol. Biol. 351*, 850–864.

41. Petkova, A. T., Leapman, R. D., Guo, Z., Yau, W. M., Mattson, M. P., and Tycko, R. (2005) Self-propagating, molecular-level polymorphism in Alzheimer's β-amyloid fibrils. *Science 307*, 262–265.

42. Makarava, N., and Baskakov, I. V. (2008) The same primary structure of the prion protein yields two distinct self-propagating states. *J. Biol. Chem. 283*, 15988–15996.

43. Kayed, R., Head, E., Thompson, J. L., McIntire, T. M., Milton, S. C., Cotman, C. W., and Glabe, C. G. (2003) Common structure of soluble amyloid oligomers implies common mechanism of pathogenesis. *Science 300*, 486–489.

44. Khurana, R., and Udgaonkar, J. B. (1994) Equilibrium unfolding studies of barstar: Evidence for an alternative conformation which resembles a molten globule. *Biochemistry 33*, 106–115.

45. Zaidi, F. N., Nath, U., and Udgaonkar, J. B. (1997) Multiple intermediates and transition states during protein unfolding. *Nat. Struct. Biol. 4*, 1016–1024.

46. Ramachandran, S., Rami, B. R., and Udgaonkar, J. B. (2000) Measurements of cysteine reactivity during protein unfolding suggest the presence of competing pathways. *J. Mol. Biol. 297*, 733–745.

47. Lakshmikanth, G. S., Sridevi, K., Krishnamoorthy, G., and Udgaonkar, J. B. (2001) Structure is lost incrementally during the unfolding of barstar. *Nat. Struct. Biol. 8*, 799–804.

48. Sridevi, K., and Udgaonkar, J. B. (2002) Unfolding rates of barstar determined in native and low denaturant conditions indicate the presence of intermediates. *Biochemistry 41*, 1568–1578.

49. Juneja, J., Bhavesh, N. S., Udgaonkar, J. B., and Hosur, R. V. (2002) NMR identification and characterization of the flexible regions in the 160 kDa molten globule-like aggregate of barstar at low pH. *Biochemistry 41*, 9885–9899.

50. Kumar, S., and Udgaonkar, J. B. (2009) Conformational conversion may precede or follow aggregate elongation on alternative pathways of amyloid protofibril formation. *J. Mol. Biol. 385*, 1266–1276.

51. Gast, K., Modler, A. J., Damaschun, H., Krober, R., Lutsch, G., Zirwer, D., Golbik, R., and Damaschun, G. (2003) Effect of environ-

mental conditions on aggregation and fibril formation of barstar. *Eur. Biophys. J. 32*, 710–723.

52. Kumar, S., and Udgaonkar, J. B. (2009) Structurally distinct amyloid protofibrils form on separate pathways of aggregation of a small protein. *Biochemistry 48*, 6441–6449.

53. Jha, A., Udgaonkar, J. B., and Krishnamoorthy, G. (2009) Characterization of the heterogeneity and specificity of interpolypeptide interactions in amyloid protofibrils by measurement of site-specific fluorescence anisotropy decay kinetics. *J. Mol. Biol. 393*, 735–752.

54. Mukhopadhyay, S., Nayak, P. K., Udgaonkar, J. B., and Krishnamoorthy, G. (2006) Characterization of the formation of amyloid protofibrils from barstar by mapping residue-specific fluorescence dynamics. *J. Mol. Biol. 358*, 935–942.

55. Nichols, M. R., Moss, M. A., Reed, D. K., Lin, W. L., Mukhopadhyay, R., Hoh, J. H., and Rosenberg, T. L. (2002) Growth of β-amyloid(1−40) protofibrils by monomer elongation and lateral association. Characterization of distinct products by light scattering and atomic force microscopy. *Biochemistry 41*, 6115–6127.

56. Teplow, D. B., Lazo, N. D., Bitan, G., Bernstein, S., Wyttenbach, T., Bowers, M. T., Baumketner, A., Shea, J. E., Urbanc, B., Cruz, L., Borreguero, J., and Stanley, H. E. (2006) Elucidating amyloid β-protein folding and assembly: A multidisciplinary approach. *Acc. Chem. Res. 39*, 635–645.

57. Jain, S., and Udgaonkar, J. B. (2010) Salt-induced modulation of the pathway of amyloid fibril formation by the mouse prion protein. *Biochemistry 49*, 7615–7624.

58. Buck, M. (1998) Trifluoroethanol and colleagues: Cosolvents come of age. Recent studies with peptides and proteins. *Q. Rev. Biophys. 31*, 297–355.

59. Munishkina, L. A., Phelan, C., Uversky, V. N., and Fink, A. L. (2003) Conformational behavior and aggregation of α-synuclein in organic solvents: Modeling the effects of membranes. *Biochemistry 42*, 2720–2730.

60. Gast, K., Siemer, A., Zirwer, D., and Damaschun, G. (2001) Fluoroalcohol-induced structural changes of proteins: Some aspects of cosolvent-protein interactions. *Eur. Biophys. J. 30*, 273–283.

61. Purcell, K. F., Stikeleather, J. A., and Brunk, S. D. (1969) Spectroscopic Studies of Hydrogen Bonding: Hexafluoroisopropanol. *J. Mol. Spectrosc. 32*, 202–213.

62. Yamaguchi, K., Naiki, H., and Goto, Y. (2006) Mechanism by which the amyloid-like fibrils of a β2-microglobulin fragment are induced by fluorine-substituted alcohols. *J. Mol. Biol. 363*, 279–288.

63. Roccatano, D., Fioroni, M., Zacharias, M., and Colombo, G. (2005) Effect of hexafluoroisopropanol alcohol on the structure of melittin: A molecular dynamics simulation study. *Protein Sci. 14*, 2582–2589.

64. Chen, S., and Wetzel, R. (2001) Solubilization and disaggregation of polyglutamine peptides. *Protein Sci. 10*, 887–891.

65. Ramachandran, S., and Udgaonkar, J. B. (1996) Stabilization of barstar by chemical modification of the buried cysteines. *Biochemistry 35*, 8776–8785.

66. Whitmore, L., and Wallace, B. A. (2004) DICHROWEB, an online server for protein secondary structure analyses from circular dichroism spectroscopic data. *Nucleic Acids Res. 32*, W668–W673.

67. Lees, J. G., Miles, A. J., Wien, F., and Wallace, B. A. (2006) A reference database for circular dichroism spectroscopy covering fold and secondary structure space. *Bioinformatics 22*, 1955–1962.

68. Horcas, I., Fernandez, R., Gomez-Rodriguez, J. M., Colchero, J., Gomez-Herrero, J., and Baro, A. M. (2007) WSXM: A software for scanning probe microscopy and a tool for nanotechnology. *Rev. Sci. Instrum. 78*, 013705.

69. Howard, J. (2001) Mechanics of Motor Proteins and the Cytoskeleton, Sinauer, Sunderland, MA.

70. Chen, B., Thurber, K. R., Shewmaker, F., Wickner, R. B., and Tycko, R. (2009) Measurement of amyloid fibril mass-per-length by tilted-beam transmission electron microscopy. *Proc. Natl. Acad. Sci. U.S.A. 106*, 14339–14344.

71. Seshadri, S., Khurana, R., and Fink, A. L. (1999) Fourier transform infrared spectroscopy in analysis of protein deposits. *Methods Enzymol. 309*, 559–576.

72. Lomakin, A., Benedek, G. B., and Teplow, D. B. (1999) Monitoring protein assembly using quasielastic light scattering spectroscopy. *Methods Enzymol. 309*, 429–459.

73. Garcia de la Torre, J. G., and Bloomfield, V. A. (1981) Hydrodynamic properties of complex, rigid, biological macromolecules: Theory and applications. *Q. Rev. Biophys. 14*, 81–139.

74. Ferrone, F. (1999) Analysis of protein aggregation kinetics. *Methods Enzymol. 309*, 256–274.

75. Srisailam, S., Kumar, T. K., Rajalingam, D., Kathir, K. M., Sheu, H. S., Jan, F. J., Chao, P. C., and Yu, C. (2003) Amyloid-like fibril formation in an all β-barrel protein. Partially structured intermediate

state(s) is a precursor for fibril formation. *J. Biol. Chem. 278*, 17701–17709.

76. Konno, T., Oiki, S., Hasegawa, K., and Naiki, H. (2004) Anionic contribution for fibrous maturation of protofibrillar assemblies of the human tau repeat domain in a fluoroalcohol solution. *Biochemistry 43*, 13613–13620.

77. Padrick, S. B., and Miranker, A. D. (2002) Islet amyloid: Phase partitioning and secondary nucleation are central to the mechanism of fibrillogenesis. *Biochemistry 41*, 4694–4703.

78. Nichols, M. R., Moss, M. A., Reed, D. K., Cratic-McDaniel, S., Hoh, J. H., and Rosenberry, T. L. (2005) Amyloid-*β* protofibrils differ from amyloid-*β* aggregates induced in dilute hexafluoroisopropanol in stability and morphology. *J. Biol. Chem. 280*, 2471–2480.

79. Hirota, N., Mizuno, K., and Goto, Y. (1998) Group additive contributions to the alcohol-induced α-helix formation of melittin: Implication for the mechanism of the alcohol effects on proteins. *J. Mol. Biol. 275*, 365–378.

80. Frieden, C. (2007) Protein aggregation processes: In search of the mechanism. *Protein Sci. 16*, 2334–2344.

81. Antony, T., Hoyer, W., Cherny, D., Heim, G., Jovin, T. M., and Subramaniam, V. (2003) Cellular polyamines promote the aggregation of α-synuclein. *J. Biol. Chem. 278*, 3235–3240.

82. Walsh, D. M., Hartley, D. M., Kusumoto, Y., Fezoui, Y., Condron, M. M., Lomakin, A., Benedek, G. B., Selkoe, D. J., and Teplow, D. B. (1999) Amyloid *β*-protein fibrillogenesis. Structure and biological activity of protofibrillar intermediates. *J. Biol. Chem. 274*, 25945–25952.

83. Rotter, M. A., Kwong, S., Briehl, R. W., and Ferrone, F. A. (2005) Heterogeneous nucleation in sickle hemoglobin: Experimental validation of a structural mechanism. *Biophys. J. 89*, 2677–2684.

84. Mirchev, R., and Ferrone, F. A. (1997) The structural link between polymerization and sickle cell disease. *J. Mol. Biol. 265*, 475–479.

85. Biancalana, M., Makabe, K., Koide, A., and Koide, S. (2009) Molecular mechanism of thioflavin-T binding to the surface of *β*-rich peptide self-assemblies. *J. Mol. Biol. 385*, 1052–1063.

86. Biancalana, M., and Koide, S. (2010) Molecular mechanism of Thioflavin-T binding to amyloid fibrils. *Biochim. Biophys. Acta 1804*, 1405–1412.

87. Wolfe, L. S., Calabrese, M. F., Nath, A., Blaho, D. V., Miranker, A. D., and Xiong, Y. (2010) Protein-induced photophysical changes to the amyloid indicator dye thioflavin T. *Proc. Natl. Acad. Sci. U.S.A. 107*, 16863–16868.

88. Chen, S., Ferrone, F. A., and Wetzel, R. (2002) Huntington's disease age-of-onset linked to polyglutamine aggregation nucleation. *Proc. Natl. Acad. Sci. U.S.A. 99*, 11884–11889.

89. Sabate, R., and Saupe, S. J. (2007) Thioflavin T fluorescence anisotropy: An alternative technique for the study of amyloid aggregation. *Biochem. Biophys. Res. Commun. 360*, 135–138.